Topological valley, pseudospin, and pseudospin-valley protected edge states in symmetric pillared phononic crystals

Wei Wang, Bernard Bonello, Bahram Djafari-Rouhani, Yan Pennec

Topological valley, pseudospin, and pseudospin-valley protected edge states in symmetric pillared phononic crystals

Wei Wang[1], Bernard Bonello[1*], Bahram Djafari-Rouhani[2], and Yan Pennec[2]

[1]Sorbonne Université, UPMC Université Paris 06 (INSP–UMR CNRS 7588),

4, place Jussieu 75005 Paris, France

[2]Institut d'Electronique, de Micro-électronique et de Nanotechnologie (IEMN–UMR CNRS 8520),

Université de Lille Sciences et Technologies, Cité Scientifique, 59652 Villeneuve d'Ascq Cedex, France

*corresponding author: bernard.bonello@insp.jussieu.fr

Abstract:

We present a symmetric double-sided pillared phononic crystal (PPnC) where either quantum spin Hall effect (QSHE) or quantum valley Hall effect (QVHE) is emulated by solely imposing different perturbations to the geometry. When occurring at the deep subwavelength scale, the valley-polarized edge state emulating QVHE becomes evanescent at the zigzag termination and can be enhanced by a locally resonant mode. When occurring at high frequency, the refracted patterns (refracted modes and angles) can be tailored. Furthermore, we demonstrate the occurrence of the pseudospin and pseudospin-valley combined edge states and the valley-dependent propagation at a T-junction constructed by PPnCs supporting QSHE and QVHE respectively.

The willingness to manipulate the propagation of elastic waves, especially Lamb waves, in phononic crystals (PnCs) by tailoring the band structures through either band folding or local resonances has been one of the most fruitful scientific pursuits in the past decades. Abnormal wave propagation phenomena, such as negative refraction, lensing, and clocking, unachievable in natural materials, have been demonstrated [1–4]. Recently, the emergence of topological insulators has provided a fascinating scheme to achieve defect-immune and lossless energy transport [5–8]. By analogy with quantum spin Hall effect (QSHE) [9–14] or quantum valley Hall effect (QVHE) [15–17], this concept was soon extended to PnCs to realize robust guiding of Lamb waves at the interface between two topologically distinct configurations. In the former case, it explores the pseudospin degree of freedom (DOF) and requires intricate designs to obtain a double Dirac cone at either Γ or K (K') points of the Brillouin zone (BZ). Usually, a double Dirac cone is easily achieved at the Γ point owing to a band folding mechanism [18–20], whereas, its occurrence at K (K') points at high frequency scale can be obtained in specifically patterned plates [21]. It has been afterwards simplified with perforated macro holes [22] which significantly reduces the geometric

complexity and further allows for the experimental observation of the pseudospin-protected edge states in continuous elastic plates. Regarding QVHE, it takes advantage of the valley DOF and only requires a single Dirac cone at the K or K' points of the BZ. This significantly simplifies both the design and the fabrication even though a large separation between two opposite valleys must be ensured to avoid the inter-valley scattering.

Very recently, the topologically protected edge state, that combines both pseudospin and valley DOFs, has gained more and more interest. Specifically, it has been reported that pseudospin-valley combined edge states can occur at the domain wall formed by two distinct configurations supporting QSHE and QVHE respectively [23–29]. Usually, these two configurations involve totally different geometries which renders their designs very complex. Therefore, designing a programmable platform that allows for swapping between QSHE and QVHE is of primary importance for this research field. Likewise, little attention has been paid to the refracted pattern of the valley-polarized edge state at the valley-conservation zigzag termination so far. Recently, an elastic phononic plate with perforated holes mimicking QVHE by either expanding or shrinking the holes and QSHE by using blind holes was reported [23]. These geometries allowed the authors to demonstrate the splitting of the equal-frequency helical edge waves in the high-frequency regime. In this work, we go a step further. By setting up pillar-shaped resonators on the perforated phononic crystal plate, the dispersion curves are significantly altered: Dirac cones in the deep subwavelength scale or at high frequency regime, and even a double Dirac cone when the dimensions are properly chosen, are achieved. We describe a symmetric double-sided PPnC where QVHE or QSHE can be emulated by merely imposing dissimilar perturbations to the geometries of the attached pillars. We demonstrate the occurrence of the valley protected, the pseudospin protected, and the pseudospin-valley combined edge states at different domain walls. When emulating QVHE, we show a variety of refracted patterns at the zigzag termination for the valley-polarized edge state including positive or negative refraction, and even evanescence. Then, we investigate the valley-dependent feature of the pseudospin-valley combined edge state and we demonstrate the valley based splitting of the pseudospin protected edge states in a T-shaped waveguide constructed by merging PPnCs supporting QSHE and QVHE respectively.

Design of the system. The unit cell of the honeycomb lattice formed by assembling two identical periodic arrays of pillars over a thin plate, together with its first irreducible BZ, are shown in Fig. 1(a). Four perforated holes are drilled at the corners of the unit cell. The lattice constant and the thickness of the plate are $a = 400\mu m$ and $e = 100\mu m$. The diameter and the height of the pillars are $d_{A,B,C,D} = D = 120$ μm and $h_{A,B,C,D} = H = 160\mu m$, and the radius of the hole is $R_H = 140$ μm. In what follows, both the plate and the pillars are made of steel whose Young's modulus, Poisson's ratio, and mass density are $E = 200$ GPa, $v = 0.3$, and $\rho = 7850$ kg/m^3, respectively.

The band structure of this double-sided PPnC, displayed in Fig. 1(b), was obtained by applying periodic conditions to the unit cell and solving the eigenvalue equations. Thanks to the symmetry about the mid-plane of the plate, it can be further decomposed into symmetric (red dotted lines) and antisymmetric (blue dotted lines) subcomponents (see the eigenmodes in Supplemental Material Fig. S1 in [30]). For comparison, the band structure of the single-sided PPnC, obtained by removing all the pillars on one side of the plate, is shown in Fig. 1(c). Clearly, two Dirac cones related to the antisymmetric branches that can be seen in Fig. 1(b) at K point of the BZ at 0.937 and 2.361 MHz persist, unlike the Dirac cone at 2.068 MHz created by the symmetric modes. In view of the wavelengths of both Lamb modes involving symmetric displacements, *i.e.* 2557 and 1513 μm for S_0 and SH_0 modes respectively, the latter Dirac cone occurs in the deep subwavelength scale and should be attributed to local resonances of the pillars. It should be noticed here that the position of the Dirac cones can be easily modified by adjusting the height of the pillars (Fig. S2 in [30]). In what follows, emphasis is placed on the Dirac cone formed by the symmetric branches, the other one being analyzed in [30].
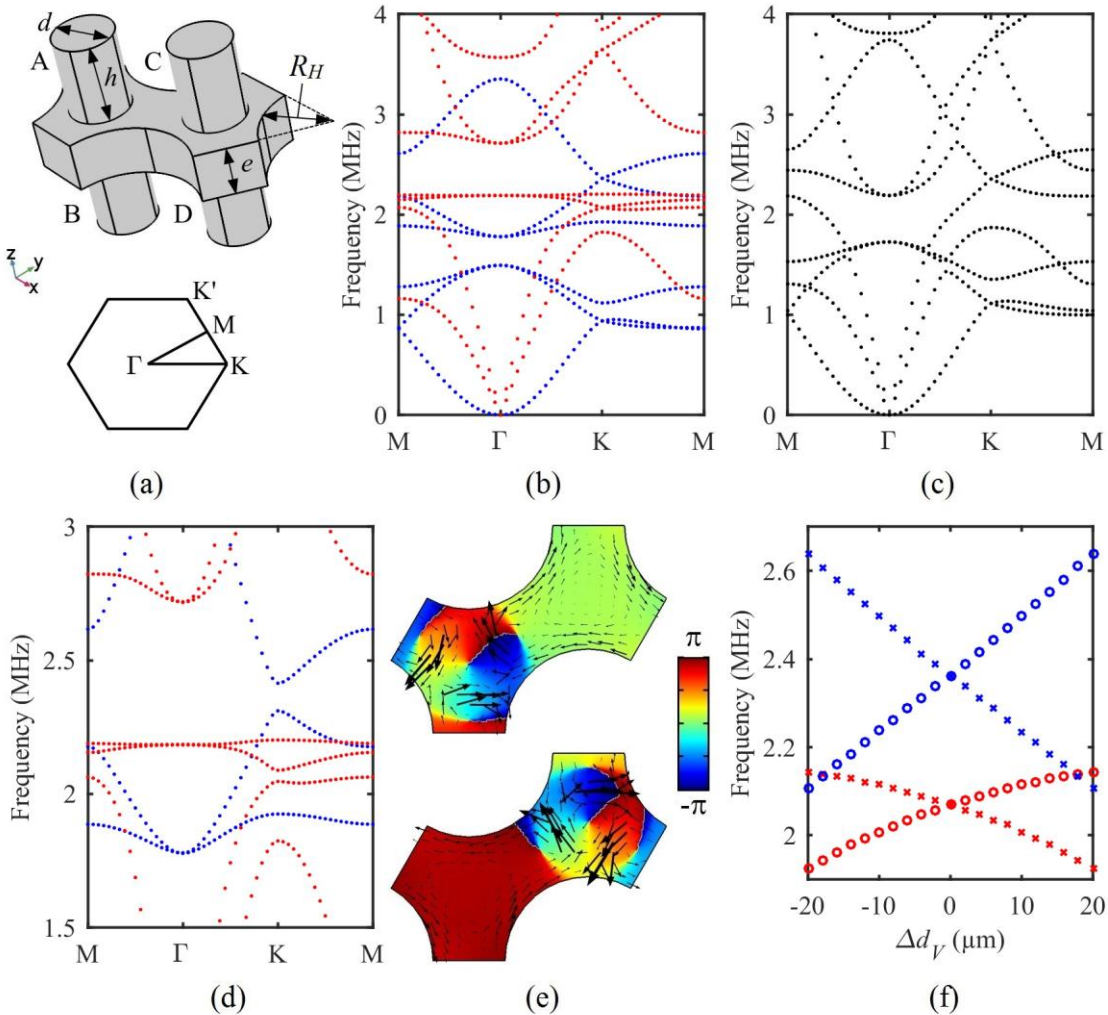
FIG. 1: (a) Elementary unit cell and its first irreducible BZ. Band structures of (b) the double-sided, (c) the single-sided and (d) the perturbed PPnCs with $\Delta d_V = 4$ µm (d). (e) Energy flux (black arrows) and phase distribution at the lower (bottom panel) and higher (top panel) bounding of the lifted Dirac cone at the valley K. (f) Evolution of the valley pseudospin states at the valley K against the perturbation. Red (blue) symbols represent the frequencies of the symmetric (antisymmetric) dispersion curves.

Valley-protected edge states. Emulating QVHE requires space-inversion symmetry (SIS) breaking in the unit cell. This can be achieved by perturbing the diameters of the pillars according to $d_{A,B} = D + \Delta d_V$ and $d_{C,D} = D - \Delta d_V$. For instance, the band structure when $\Delta d_V = 4$ µm, which corresponds to a small SIS breaking case, is displayed in Fig. 1(d). Both Dirac cones get lifted, which leads to two nontrivial band gaps. Regarding the symmetric branches, the energy flux, together with the phase distribution on the top surface of the plate at the lifted Dirac cone are depicted in Fig. 1(e). It unambiguously reveals the vortex chirality and the corresponding modes can therefore be recognized as valley pseudospin states. The topological features associated with the antisymmetric dispersion curves are handled in [30] [see Fig. S3(a)]. Figure 1(f) shows the dependence of the valley pseudospin states against the diameter perturbation with the red and blue crosses (circles) representing the valley pseudospin down (up) states. When crossing zero, their frequency order is inverted and the band gap at first closes and then reopens, which is the signature of the topological phase transition. At the same time, the valley Chern number defined as the integral of the Berry curvature in the vicinity of the valley becomes nonzero. Theoretically, it converges quickly to $C_V(K/K') = \pm 1/2$ for the lower bounding. The corresponding numerical demonstrations are displayed in Fig. S3(c) in [30].

The most suitable way to investigate the edge states is to consider the three-layer ribbon supercell shown in Fig. 2(a). It is built by sandwiching eight unit cells with perturbation $\Delta d_V = -10$ µm, in between two sets of six unit cells, each of them with perturbation $\Delta d_V = +10$ µm. This supercell features two different zigzag domain walls of type SDW and LDW with adjacent pillars having respectively small and large diameters. (Table 1 below summarizes the geometries we investigate in this work). The projection of the valleys K and K' on these domain walls is $k_x = -2\pi/3a$ and $k_x = 2\pi/3a$, respectively. Three branches appear in the reopened band gap, as shown in Fig. 2(b). The eigenmodes at $k_x = 0.5\pi/a$ are also displayed in Fig. 2(b). The magenta and cyan dotted lines represent the edge states occurring at SDW and LDW respectively whereas the black dotted line is the locally resonant mode at the bottom end where the pillars with a large diameter are placed at the extreme end of the supercell (see the zoomed view in the inset).

Let us now consider the propagation of the K'-polarized edge state along SDW and its refraction at the zigzag termination. To this end, a left-going wave at 2.042 MHz is excited by two phase-matched sources [31] and the displacement field on the top surface of the plate is recorded. The in-plane component is

4

plotted in Fig. 2(c) (see Fig. S7 in [30] for the out-of-plane component). The edge state, which is mainly SH polarized, turns downwards and remains mostly localized at the interface, even though some elastic energy is spread across the plate and a small portion propagates along the bottom interface. The equifrequency contours (EFCs) shown in the inset of Fig. 2(d) allow one to interpret this mapping. The deformation associated to the edge state having the mirror symmetry, only the S_0 and SH_0 Lamb modes should be considered; the corresponding EFCs are represented in Fig. 2(d) by the red and green solid lines respectively. The two cyan dashed lines represent the normal to the zigzag termination. The edge state is locked to three K' valleys (black dots) in the BZ (black solid line). The wave vector in the plate can be graphically obtained owing to the conservation of the component of the wave vector parallel to the interface. Obviously, it is imaginary and the refracted wave is thus evanescent. However, due to the coupling with the locally resonant mode occurring at the edges ending with pillars having a large diameter [see the zoomed view in the inset of Fig. 2(c)], the magnitude of the evanescent wave is strongly enhanced. In contrast, there is no vibration enhancement if the resonant pillars (highlighted in blue in the zoom) are removed, as shown in Fig. 2(d). This well explains that the magnitude at the bottom interface is nearly zero. It should be noticed that such a behavior may be fairly different from the refraction scheme undergone by TE and TM electromagnetic modes at the outlet of a photonic crystal having a quite similar geometry. Actually, instead of the evanescence of the elastic modes observed here, the photonic structure made of metallic cylindrical rods in between two parallel plates described in Ref. [26] allows for the anomalous refraction, while in a different manner, of both TE and TM optical modes.

Note that another Dirac cone occurs at 5.916 MHz in the symmetric dispersion curves when the height of the pillars is reduced down to 80 µm. In that case, the edge state refracts into both S_0 and SH_0 Lamb waves (see Figs. S10 and S11 in [30] for details). More interestingly, for the valley-polarized edge state of the antisymmetric dispersion curves, the refracted pattern consists of one or two A_0 Lamb modes at the zigzag termination and one or three A_0 Lamb modes at the armchair termination, depending on the height of the pillars (see Figs. S4, S5, and S6 in [30]).
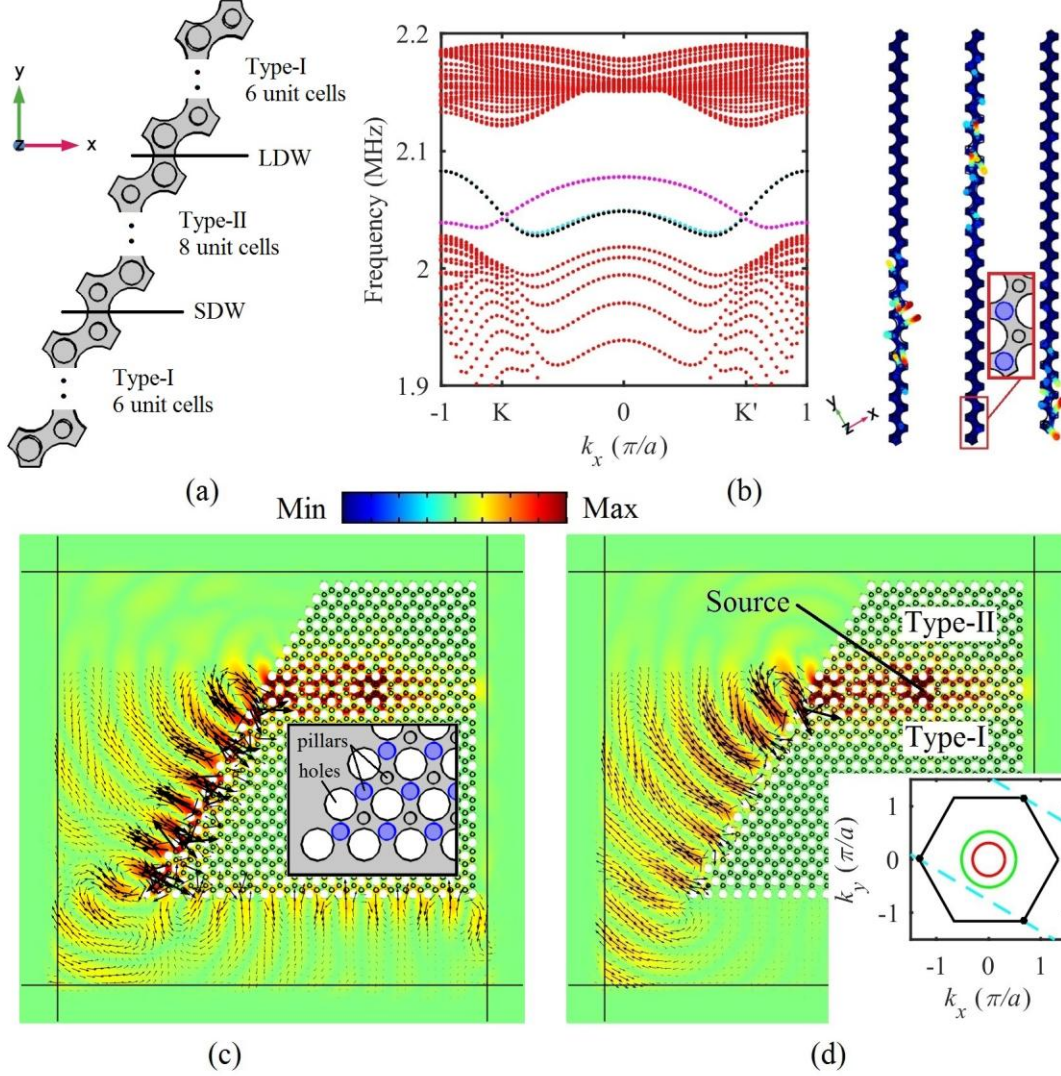
FIG. 2: (a) Schematic of the three-layer ribbon supercell constructed by type-I ($\Delta d_V = 10$ μm) and type-II ($\Delta d_V = -10$ μm) PPnCs. (b) Symmetric dispsersion curves of the supercell and the eigenmodes of the edge states (magenta and cyan branches) and locally resonant mode (black branch) at $k_x = 0.5\pi/a$ with a zoomed view of the undeformed supercell at the bottom end. Plots of the magnitude of the in-plane displacement on the top surface of the plate (c) with and (d) without the resonant pillars at the interfaces. Inset in (c): zoomed view at the left bottom corner. Inset in (d): EFCs anlysis.

Pseudospin-protected edge states. The proximity of the Dirac cones in the symmetric and antisymmetric dispersion curves in the BZ suggests that they might overlap if the dimensions of the unit cell are properly designed, giving rise to a double Dirac cone and thus to emulation of QSHE. This is indeed the case when $d_{A,B,C,D} = D = 80$ μm, $h_{A,B,C,D} = H = 153.6$ μm, and $e = 70$ μm, as shown in Fig. 3(a). If moreover, one imposes the perturbation with $h_{A,D} = H + \Delta h_S$ and $h_{B,C} = H - \Delta h_S$, the mirror symmetry about the midplane in the unit cell is broken. The symmetric and antisymmetric modes hybridize near the original double Dirac cone which introduces the emulation of the spin-orbit coupling interaction. Within this

framework, the in-phase and out-of-phase hybridization can be used as the effective up and down pseudospin states respectively [21]. The band structure for $\Delta h_S = 3$ µm (type-III) is shown in Fig. 3(b). The double Dirac cone splits into two single ones and a nontrivial complete band gap reopens. Furthermore, the comparison with Fig. 3(a) shows that the lower (upper) Dirac cone combines the lower (upper) symmetric and antisymmetric modes. The eigenmodes at the two Dirac cones shown in the right panel of Fig. 3(b) illustrate the pairwise hybridization.

The spin Chern numbers $C_S^{\uparrow\downarrow}(\text{K/K'}) = \mp 1/2$ were derived from the integration of the Berry curvature of the four constitutive branches around the valley K (Fig. S12 in [30]). Therefore, the juxtaposition with another PPnC whose height of pillars is reduced by $\Delta h_S = -3$ µm (type-IV), allows for pseudospin protected edge states at the domain wall, as shown in Fig. 3(c). The spin Chern number difference ± 1 at each valley guarantees that two spin-locked pairs of edge state occur in the reopened band gap, namely, a forward spin-down ($\downarrow$) pair (cyan dotted lines) and a backward spin-up ($\uparrow$) pair (magenta dotted lines). Figure 3(d) shows the propagation of the spin-locked edge states at 1.782 MHz at the valley K, the harmonic source being located in the middle of the domains limit. Both the left-going (spin-up) and right-going (spin-down) waves are excited, which is consistent with the two available edge states. The refracted patterns at the left and right zigzag terminations predicted by EFCs analysis are depicted in Fig. 3(d). In the analysis, owing to the mirror symmetry breaking in the perturbed configuration, all three Lamb modes are assumed. Due to the extremely small wave vectors of S_0 and SH_0 Lamb modes in the plate, the edge state can only undergo refraction into A_0 Lamb mode. The wave vectors of the refracted beams [blue bold arrows in Fig. 3(d)] are in good agreement with the out-of-plane displacement field at both terminations.
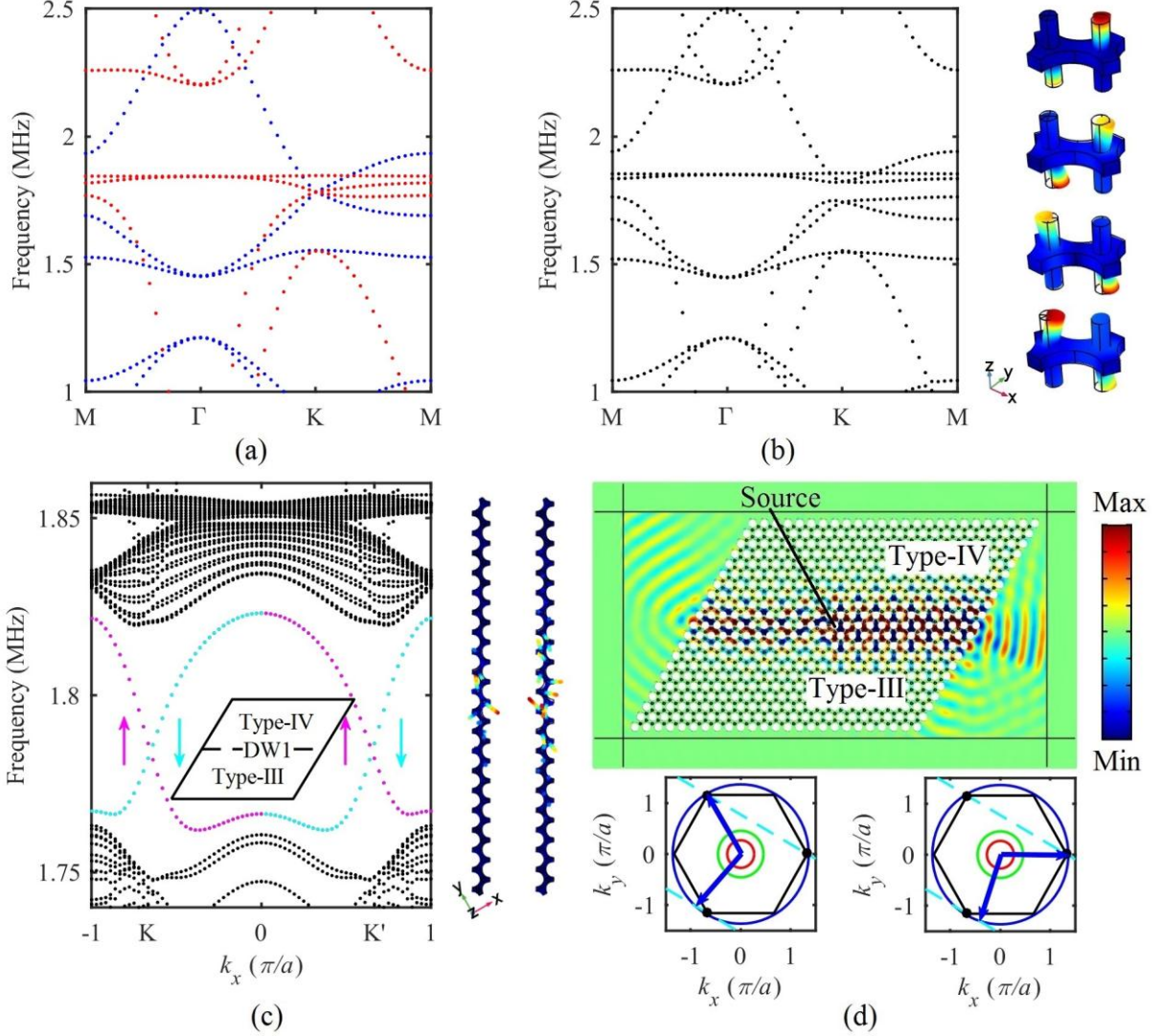
FIG. 3: (a) Occurrence of the double Dirac cone for specific dimensions (see text). (b) Band structure of the perturbed PPnC with $\Delta h_S = 3$ μm and the eigenmodes at two Dirac cones. (c) Dispersion curves of the two-layer ribbon supercell constructed by type-III and type-IV PPnCs and the eigenmodes of the edge states (magenta and cyan branches) at $k_x = 0.5\pi/a$. (d) Plot of the out-of-plane displacement on the top surface of the plate and the refracted patterns at the left and right zigzag terminations predicted by EFCs analysis.

Pseudospin-valley combined edge states. Depending on the perturbation imposed on the diameter or the height of the pillars, reserving or breaking the mirror symmetry about the mid-plane of the plate, the system may emulate either QVHE or QSHE. It provides therefore a unique opportunity to investigate the pseudospin-valley combined edge state that utilizes both pseudospin and valley DOFs to control the wave propagation, unlike the valley-dependent propagation in Fig. 2(b) and the spin-locked propagation in Fig. 3(c). Figure 4(a) shows the dispersion curves of a two-layer ribbon supercell (see the inset) built by PPnCs with $\Delta h_S = -3$ μm (type IV) emulating QSHE and $\Delta d_V = -4$ μm (type V) emulating QVHE. At the valley

K, the valley Chern number of type-V PPnC is $C_V^{\uparrow\downarrow}(K) = -1/2$ whereas the spin Chern number of type IV PPnC is $C_S^{\uparrow\downarrow}(K) = \pm 1/2$. The magenta dotted line denotes the backward spin-up edge state along DW2, where the Chern numbers difference is equal to −1. Similarly, at the valley K', the cyan dotted line represents the forward spin-down edge state occurring along this interface. The corresponding eigenmode is displayed in the right panel. Therefore, the propagation of the edge states is determined both by the pseudospin and by the valley states. The gray dotted steep lines in Fig. 4(a) represent the modes localized at the bottom end of the lower layer that is designed to emulate QVHE (see the eigenmode shown in the right panel). They are similar to the locally resonant modes represented by the black dotted line in Figs. 2(b) and S4. Figure 4(b) shows the dispersion curves of another two-layers ribbon supercell (see the inset) built by PPnCs with $\Delta h_S = 3$ μm (type III) and $\Delta d_V = -4$ μm (type V). It should be mentioned that the projection of the valleys K and K' on this domain wall now changes to be $k_{x'} = 2\pi/3a$ and $k_{x'} = -2\pi/3a$ respectively. Along DW3, a forward spin-up edge state occurs at the valley K' (magenta dotted line), whereas a backward spin-down edge state occurs at the valley K (cyan dotted line). Clearly, the propagation of the spin-down edge state along DW2 and DW3 depends on the specific valley. Considering the T-shaped wave guide displayed in Fig. 4(c), the spin-down edge state localized at both valleys [$\psi^{\downarrow}(K/K')$] can propagate along DW1, as discussed above and summarized in Fig. 3(c), whereas it is locked to the valley K' [$\varphi^{\downarrow}(K')$] along DW2 and to the valley K [$\varphi^{\downarrow}(K)$] along DW3. Therefore, the valley based splitting of the pseudospin-protected edge state should be expected at the junction.

To confirm this, the pseudospin protected edge states at 1.782 MHz are selectively excited at the valley K [31]. The resulting out-of-plane displacement field is displayed in Fig. 4(d). Both the left-going spin-up edge state and the right-going spin-down edge state are generated. Upon encountering the junction, the spin-down state propagates downwards along DW3. Vice versa, when the wave vector is locked to the valley K', as shown in Fig. 4(e), the right-going spin-down state only propagates along DW2. Unambiguously, the system allows for the valley based splitting of the spin-down edge states.
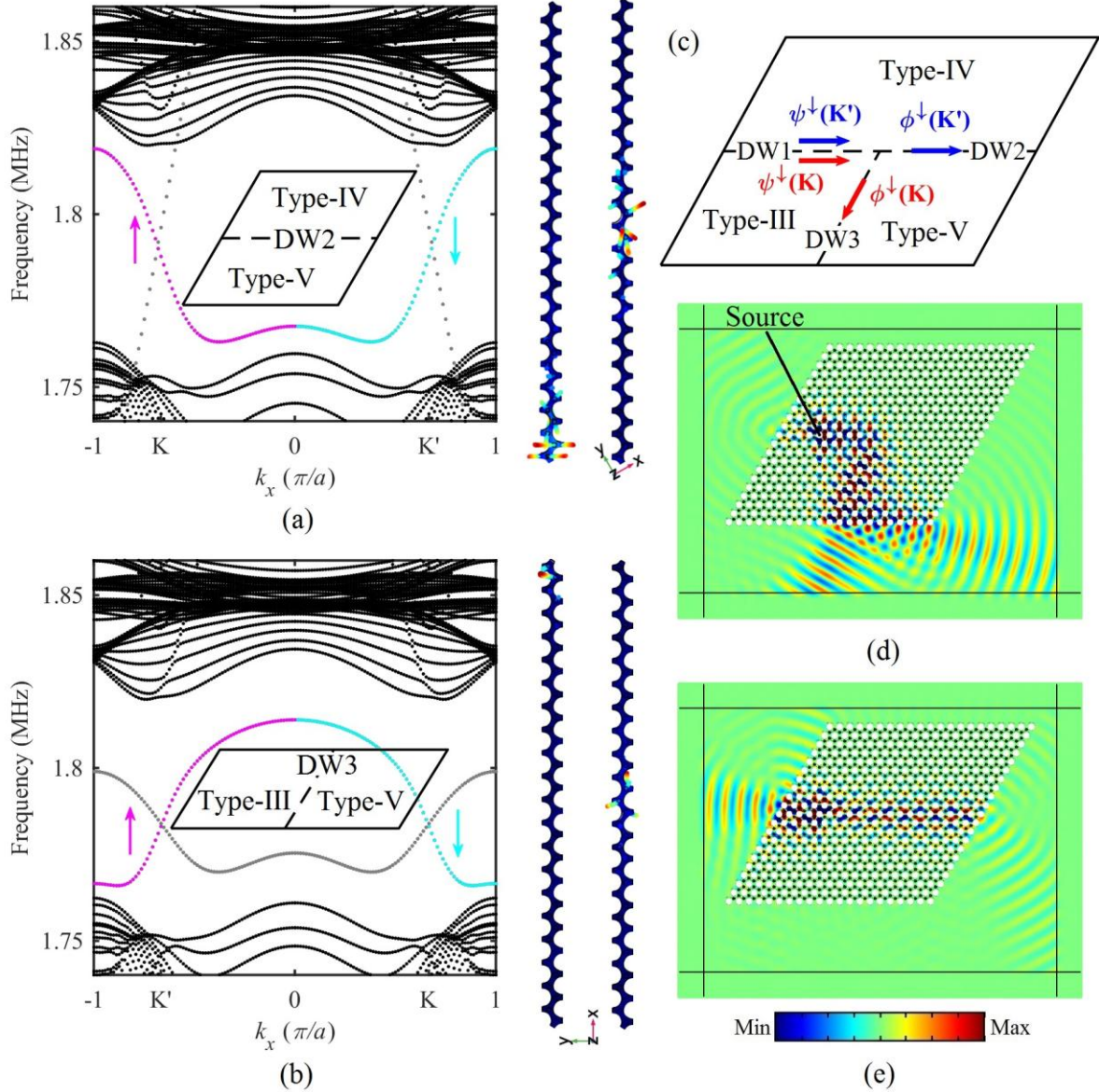
FIG. 4: Dispersion curves of two two-layer ribbon supercells built by (a) type-IV and type-V PPnCs and (b) type-III and type-V PPnCs respectively and the corresponding eigenmodes of the localized modes (grey branches) and edge states (cyan branche) at $k_x = 2\pi/3a$. (c) Schematic of the T-shaped wave guide and the valley based splitting of the spin-down edge state. Plots of the out-of-plane displacement on the top surface of the plate while the pseudospin-protected edge states are locked to (d) the valley K and (e) K' respectively.

In conclusion, we have demonstrated in this Rapid Communication that the proposed symmetric double-sided PPnC can emulate both QVHE and QSHE by solely imposing different geometric perturbations. When QVHE is emulated, the type of refracted Lamb modes as well as the angles of the valley-polarized edge states at the zigzag and armchair terminations can be tailored through a proper choice of the height of the pillars. Specifically, in the deep subwavelength scale, the edge state becomes evanescent and can be enhanced by the locally resonant mode at the interface. By optimizing the geometrical parameters of the

unit cell, a double Dirac cone can be obtained. We put into evidence the occurrence of the pseudospin protected edge state, in analogy to QSHE. Furthermore, we have demonstrated the valley-dependent feature of the pseudospin-valley combined edge state and the valley based splitting of the pseudospin-protected edge states in a T-shaped wave guide.

Table 1: Parameters of the PPnCs emulating QVHE or QSHE.

	PPnCs	Unperturbed pillar height H (µm)	Unperturbed pillar diameter D (µm)	Plate thickness e (µm)	Perturbation (µm)	Hole radius R_H (µm)
QVHE	Type-I	160	120	100	$\Delta d_V = 10$	140
	Type-II	160	120	100	$\Delta d_V = -10$	140
	Type-V	152.5	80	70	$\Delta d_V = -4$	160
QSHE	Type-III	153.6	80	70	$\Delta h_S = 3$	160
	Type-IV	153.6	80	70	$\Delta h_S = -3$	160

References:

[1]   A. Sukhovich, B. Merheb, K. Muralidharan, J. O. Vasseur, Y. Pennec, P. A. Deymier, and J. H. Page, Phys. Rev. Lett. **102**, 154301 (2009).

[2]   M. Farhat, S. Guenneau, and S. Enoch, Phys. Rev. Lett. **103**, 024301 (2009).

[3]   R. Zhu, X. N. Liu, G. K. Hu, C. T. Sun, and G. L. Huang, Nat. Commun. **5**, 5510 (2014).

[4]   W. Wang, B. Bonello, B. Djafari-Rouhani, Y. Pennec, and J. Zhao, Phys. Rev. Appl. **10**, 064011 (2018).

[5]   M. Z. Hasan and C. L. Kane, Rev. Mod. Phys. **82**, 3045 (2010).

[6]   Z. Yang, F. Gao, X. Shi, X. Lin, Z. Gao, Y. Chong, and B. Zhang, Phys. Rev. Lett. **114**, 114301 (2015).

[7]   A. Bansil, H. Lin, and T. Das, Rev. Mod. Phys. **88**, 021004 (2016).

[8]   G. Ma, M. Xiao, and C. T. Chan, Nat. Rev. Phys. **1**, 281 (2019).

[9]   Y. Guo, T. Dekorsy, and M. Hettich, Sci. Rep. **7**, 18043 (2017).

[10]   S. Y. Huo, J. J. Chen, and H. B. Huang, J. Phys. Condens. Matter **30**, 145403 (2018).

[11]   S.-Y. Yu, C. He, Z. Wang, F.-K. Liu, X.-C. Sun, Z. Li, H.-Z. Lu, M.-H. Lu, X.-P. Liu, and Y.-F. Chen, Nat. Commun. **9**, 3072 (2018).

[12]   S. Li, D. Zhao, H. Niu, X. Zhu, and J. Zang, Nat. Commun. **9**, 1370 (2018).

[13]   R. Chaunsali, C. W. Chen, and J. Yang, Phys. Rev. B **97**, 054307 (2018).

[14]   A. Foehr, O. R. Bilal, S. D. Huber, and C. Daraio, Phys. Rev. Lett. **120**, 205501 (2018).

[15]   J. Vila, R. K. Pal, and M. Ruzzene, Phys. Rev. B **96**, 134307 (2017).

[16]   M. Yan, J. Lu, F. Li, W. Deng, X. Huang, J. Ma, and Z. Liu, Nat. Mater. **17**, 993 (2018).

[17]   Y. Jin, D. Torrent, and B. Djafari-Rouhani, Phys. Rev. B **98**, 054307 (2018).

[18]   L.-H. Wu and X. Hu, Phys. Rev. Lett. **114**, 223901 (2015).

[19]   Z. Zhang, Q. Wei, Y. Cheng, T. Zhang, D. Wu, and X. Liu, Phys. Rev. Lett. **118**, 084303 (2017).

[20]   Y. Yang, Y. F. Xu, T. Xu, H. X. Wang, J. H. Jiang, X. Hu, and Z. H. Hang, Phys. Rev. Lett. **120**, 217401 (2018).

[21]   S. H. Mousavi, A. B. Khanikaev, and Z. Wang, Nat. Commun. **6**, 8682 (2015).

[22]   M. Miniaci, R. K. Pal, B. Morvan, and M. Ruzzene, Phys. Rev. X **8**, 031074 (2018).

[23]   M. Miniaci, R. K. Pal, R. Manna, and M. Ruzzene, Phys. Rev. B **100**, 024304 (2019).

[24]   Y. Kang, X. Cheng, X. Ni, A. B. Khanikaev, and A. Z. Genack, Nat. Commun. **9**, 3029 (2018).

[25]   X. Ni, D. Purtseladze, D. A. Smirnova, A. Slobozhanyuk, A. Alù, and A. B. Khanikaev, Sci. Adv. **4**, eeap8802 (2018).

[26]   F. Gao, H. Xue, Z. Yang, K. Lai, Y. Yu, X. Lin, Y. Chong, G. Shvets, and B. Zhang, Nat. Phys. **14**, 140 (2018).

[27]   Y. Chen, X. Liu, and G. Hu, J. Mech. Phys. Solids **122**, 54 (2019).

[28]   T. Ma and G. Shvets, Phys. Rev. B **95**, 165102 (2017).

[29]   C. He, S.-Y. Yu, H. Ge, H. Wang, Y. Tian, H. Zhang, X.-C. Sun, Y. B. Chen, J. Zhou, M.-H. Lu,

and Y.-F. Chen, Nat. Commun. **9**, 4555 (2018).

[30]   See Supplemental Material for additional information on the eigenmodes of the symmetric and antisymmetric dispersion curves, their evolution against the height of the pillars, topologial phase transition when emulating QVHE and QSHE, tunable refraction of the valley-polarized edge states and parameters for PPnCs.

[31]   T. W. Liu and F. Semperlotti, Phys. Rev. Appl. **9**, 014001 (2018).